Pannexin-2 deficient zebrafish develop ocular and visual motor behaviour defects

Authors: *Riya Shanbhag[§1,4], Georg S.O. Zoidl[$1,4], Shiva Sabour[$2], Fatema Nakhuda[1,4], Christiane Zoidl[3,4], Armin Bahl[5], Nima Tabatabaei[2], Georg R. Zoidl[1,3,4]*

Affiliations:

[1]Biology, [2]Engineering, [3]Psychology, [4]Center for Integrated and Applied Neuroscience, York University, Canada; [5]Centre for the Advanced Study of Collective Behaviour, University of Konstanz, Germany

[$] equal contributions

Corresponding Author: Riya Shanbhag[§] (riya28@yorku.ca)

Abstract

Pannexin-2 (Panx2), unlike the other pannexin channels Panx1 and Panx3, exhibits a unique intracellular distribution, localizing at ER-mitochondria contact sites. These specialized microdomains are crucial for important cellular functions, including calcium homeostasis, lipid transfer, inflammation, and apoptosis. Despite their presence in neurons and glial cells, the function of Panx2 at ER-mitochondria contact sites in neurotransmission remains unclear. Here, we used TALEN technology to develop a *Panx2* knockout (*Panx2*$^{-/-}$) zebrafish model, to investigate its role in neuronal communication. In 6 days, post fertilization TL (*Panx2*$^{+/+}$) larvae, Panx2 expression was observed in the inner and outer plexiform layers of the retina and the arborization fields of the optic tract. Transcriptome profiling of *Panx2*$^{-/-}$ larvae by RNA-seq analysis revealed down-regulation of vision-related genes, specifically those involved in visual and sensory perception and lens development. Behavioral tests showed that loss of Panx2 leads to altered visual motor response (VMR); *Panx2*$^{-/-}$ larvae exhibited reduced locomotor activity during light phases and increased activity during dark phases. Additionally, the knockout larvae displayed significantly impaired optomotor response (OMR). When we tested the geometric and refractive properties of adult eyes, optical coherence tomography (OCT) analysis of *Panx2*$^{-/-}$ fish revealed a longer mean axial length and a negative shift in retinal refractive error (RRE) values, both indicative of myopia. Furthermore, the increased corneal thickness observed in *Panx2*$^{-/-}$ fish corroborated the molecular and behavioural alterations. Our findings highlight a novel role of Panx2 in retinal development, visual perception, and ocular health.

Introduction

Pannexin-2 is the least studied member of the vertebrate-specific family of three proteins Pannexin-1 (Panx1), Pannexin-2 (Panx2), and Pannexin-3 (Panx3) (1). Early reports demonstrated that mammalian Panx2 exhibited a particularly dynamic expression pattern, with low levels during prenatal development and a significant increase postnatally, suggesting its involvement in CNS expansion (2). In line with this, another early report pointed toward a role of Panx2 in regulating the timing of neuronal differentiation, via an S-palmitoylated modification (3). Although originally believed to be confined to the central nervous system (4–6), Panx2 has since been detected in sixteen different tissues; highest in skin, skeletal muscles, and the eye (7). Recent structural studies have revealed Panx2 as a channel-forming protein with a unique pore architecture that allows the passage of small molecules, including ATP (8,9). The protein undergoes post-translational modifications, including N-glycosylation at asparagine (N86) within its first extracellular loop (10). Unlike Panx1 and Panx3, N-glycosylated Panx2 is absent from the plasma membrane (11,12). While Panx2 was known to localize within the cytoplasm, its specific organelle distribution was not consistently defined. Studies reported its presence in various intracellular structures, including the ER, Golgi apparatus, and endolysosomes (10,13,14). Notably, Le Vasseur et al. identified Panx2 as a novel component of mitochondria-associated membranes (MAMs), using compelling live-cell imaging and electron microscopy (15). The authors showed that approximately 60% of endogenous Panx2 directly associates with mitochondria under physiological conditions, suggesting specialized roles that differentiate it from other pannexins. MAMs are dynamic ER-mitochondria contact sites crucial for cellular processes such as lipid transfer, calcium homeostasis, immune regulation, and cell death (16). We know that there are numerous ER-mitochondria contact sites in neurons (17), however the

specific roles of Panx2 within these junctions, particularly in the context of neurotransmission, neurodegenerative diseases, and cancer remains to be elucidated (18,19).

Multiple Panx2 isoforms exist in humans and zebrafish, with conserved regions primarily localized within the transmembrane domains and intracellular loops (6). Notably, the Panx2 C-terminal domain exhibits significant sequence variation compared to Panx1 and Panx3 (9). To investigate whether these paralog differences correlate with distinct expression patterns, we performed HCR-fluorescent *in situ* hybridization of whole larval zebrafish. Our results revealed P*anx2* mRNA expression in regions of the forebrain, cerebellum, and optic tectum. To further elucidate the role of Panx2 in neuronal communication and MAMs function, we generated a global Panx2 knockout zebrafish model using TALEN technology. A custom-made antibody identified Panx2 in the inner segments of photoreceptors and the outer retina and confirmed the loss of Panx2 in the knockout. Transcriptome analysis revealed differential expression of genes involved in visual perception, circadian rhythm, and both innate and adaptive immune responses. Subsequent behavioral studies demonstrated that loss of Panx2 impairs visual motor responses and optomotor behavior, highlighting its critical role in visual information processing. Lastly, optical coherence tomography of adult zebrafish eyes revealed alterations in the shape and size of the lens and eye, suggesting that early-life molecular changes induced by the absence of Panx2 result in a myopia-like phenotype. We concluded that Panx2's novel association with myopia is a contributing factor to the observed visual-motor phenotype.

Results

Panx2 is expressed broadly in the brain of zebrafish larvae.

RNA fluorescence in-situ hybridization (RNA-FISH) was used to determine *panx2* expression in 6 days post-fertilization (dpf) whole-mount TL larvae. We found *panx2* mRNA widely expressed in the forebrain, cerebellum, optic tectum and retina **(Fig. 1)**.

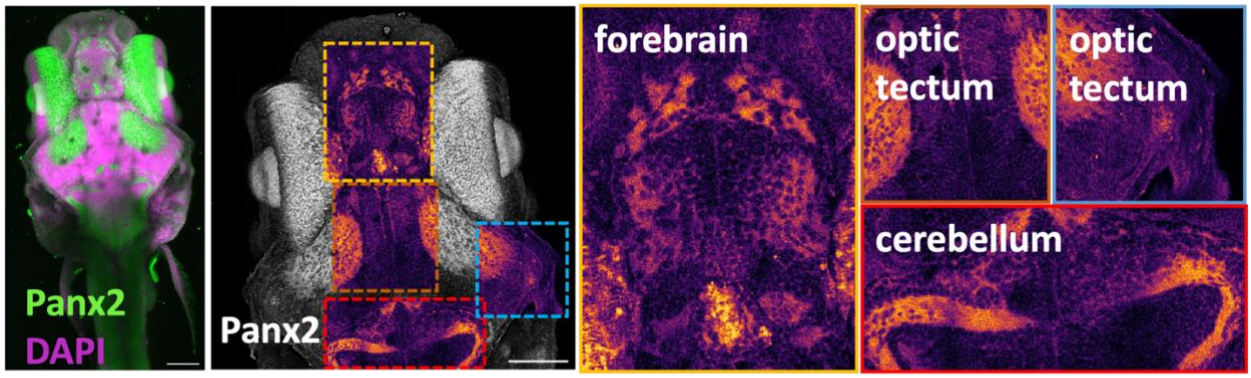

Figure 1: panx2 is expressed broadly in the brain of zebrafish larvae**.** The spatial distribution of panx2 mRNA was detected by fluorescence in-situ hybridization. Scale bars:100 µm.

Generating a Panx2 global knockout zebrafish line.

The *panx2* mutant allele was generated by TALEN-mediated genome editing, targeting the *BamHI* restriction endonuclease site in the first exon of the *panx2 gene* **(Fig. 2a)**. A DNA sequence analysis of microinjected embryos identified short 4 to 11 base pairs (bp) long nucleotide deletions in exon one of the *panx2* gene. An adult founder fish (F0) with a 11 base pair deletion (*panx2*Δ11) was selected for further experimentation **(Fig. 2b)**. In this fish the 11 bp deletion caused a frameshift at amino acid (aa) G28, resulting in a premature stop codon. The consequence of this stop codon was a truncated reading frame for a 27-aa protein, lacking 640-aa of the 651-aa long Panx2-C protein sequence **(Fig. 2c)**. The *Panx2*$^{-/-}$ fish were viable and breed for multiple generations. When comparing age-matched male and female adults to wild type siblings a modest but significant decrease in body length was noted **(Fig. 2d,e)**. The gene-editing event in exon1 effectively eliminated the shared start codon for the three known Panx2 protein isoforms A: 580-aa (ABY78016), B: 604-aa (ABY78018), and C: 651aa (ABY78017). The Panx2-C isoform was the most abundant Panx2 mRNA detectable in 6 dpf TL (*Panx2*$^{+/+}$) larvae by RT-qPCR suggesting that it may play a dominant role in Panx2-mediated functions (**Fig. 2f**).

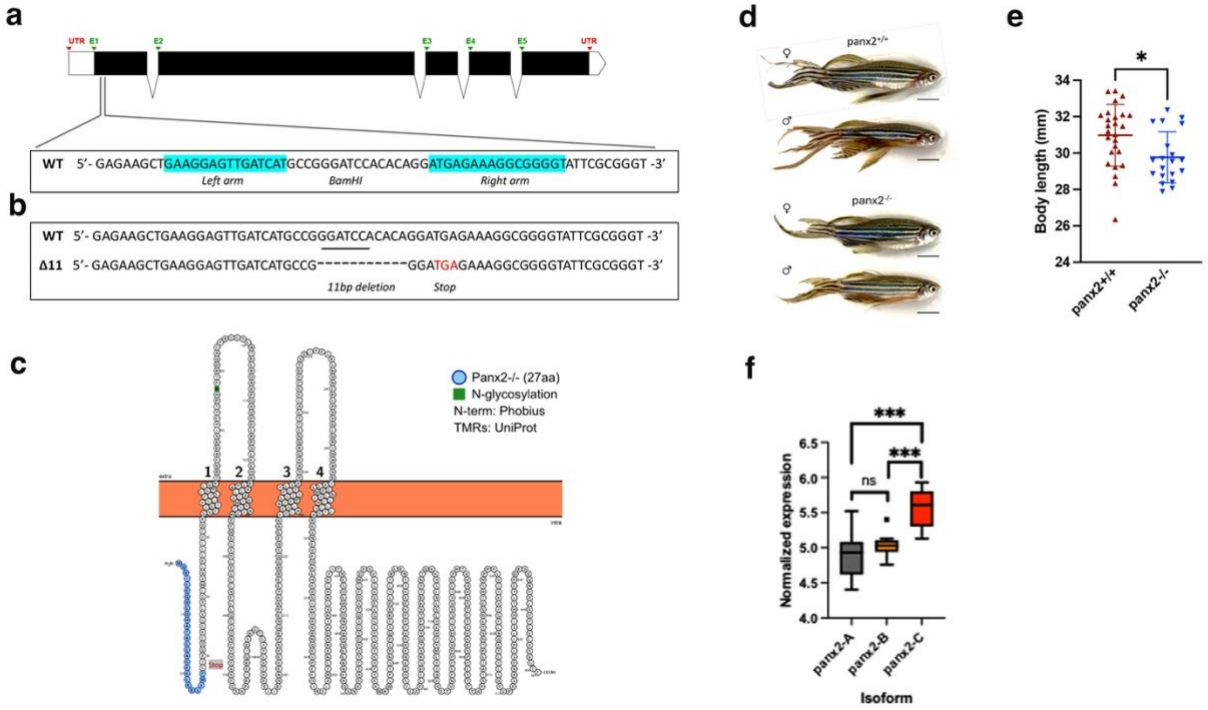

Figure 2: Generating a Panx2 global knockout zebrafish line. a) Exon-intron organization of the zebrafish Panx2 gene (ENSDARG00000063019, chromosome 18 (GRCz11:CM002902.2). The positions of the targeting Left and Right arms with a unique BamHI restriction endonuclease site in a spacer region between the TALEN pair are highlighted. b) Representation of the 11bp deletion causing a premature stop codon. c) Graphical representation of the predicted Panx2 structure. The region in blue indicates the residual sequence of 27 amino acids followed by a new in-frame stop codon. d,e) Comparison of the body length of age-matched adult zebrafish of both sexes. f) Real Time PCR quantification and presentation of the normalized expression of the three Panx2 isoforms. Statistics in e,f: Welch's test. Sample sizes were n=26 for *Panx2*$^{+/+}$ and n=20 for *Panx2*$^{-/-}$. Significance: ***P-value<0.001 and *P-value<0.05. Error bars = SD.

Panx2 is localized in the outer retina of the zebrafish.

To demonstrate the loss of Panx2 protein expression in larvae a custom polyclonal anti-peptide Panx2 antibody was generated. *Panx2*$^{+/+}$ larvae revealed a low, ubiquitous Panx2 immunoreactivity, which was most pronounced in the outer retina, the inner plexiform layer, and the lens epithelium (**Fig. 3a, see open triangles**). Panx2 knockout larvae exhibited a significant reduction in fluorescence with residual signals attributed to collagen autofluorescence in the sclera and at the margins of the lens epithelium (**Fig. 3b**). At higher magnification of the outer retina Panx2 localization was prominent in the axons of the inner segments of photoreceptor cells

and the lens epithelium (**Fig. 3c,d, see open triangles**). No immunoreactivity was detected in horizontal cells which express two other pannexins, the Panx1a and Panx1b isoforms (Prochnow et al. (2012).

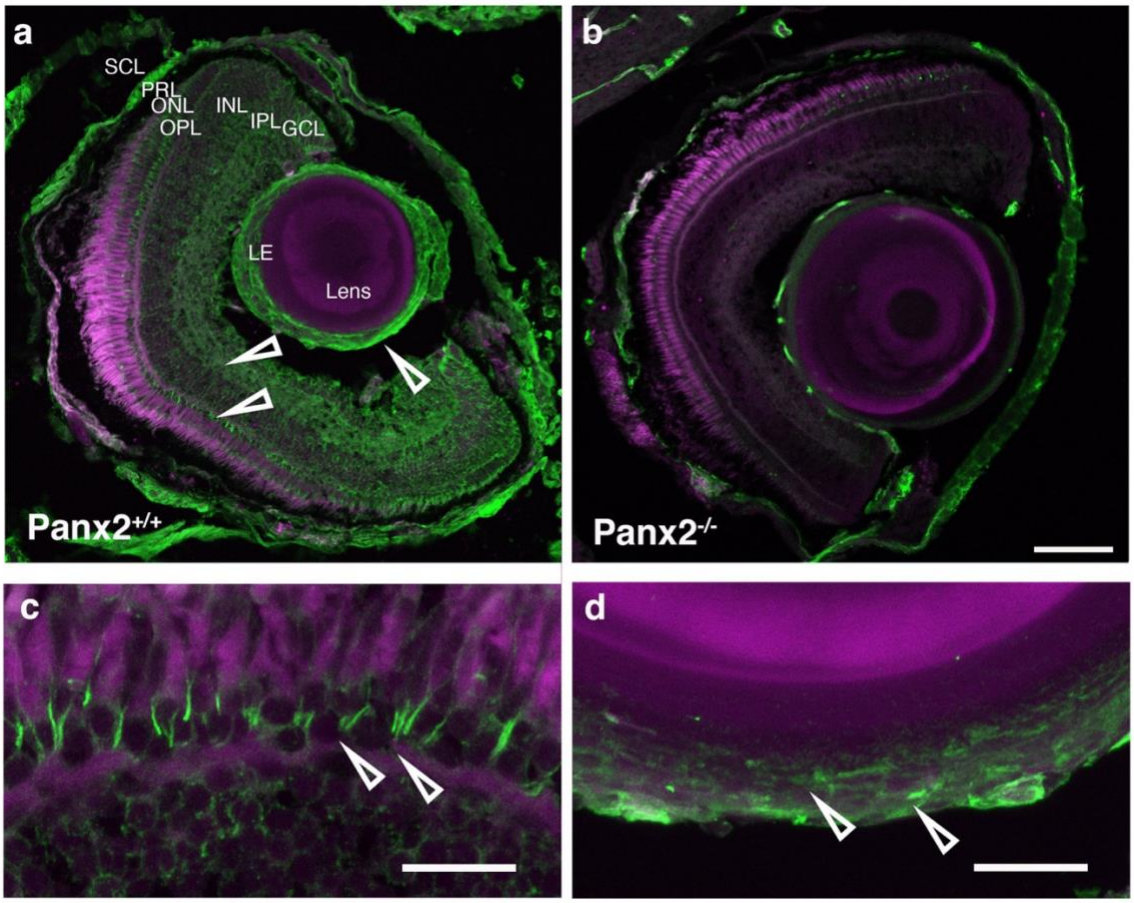

Figure 3: Panx2 localization in outer retina of the zebrafish. a) Panx2 proteins are ubiquitously expressed throughout the retina. The expression was enriched in the outer retina, the inner plexiform layer, and the lens epithelium. b) After Panx2 ablation the expression was greatly reduced across the retina, with residual staining left in tissue known for high autofluorescence. c) Higher magnification of the outer retina showing the pronounced staining in sections of the inner photoreceptor segments. d) Higher magnification of the lens epithelium. Abbreviations: SCL sclera, LE lens epithelium, GCL ganglion cell layer, IPL inner plexiform layer, INL inner nuclear layer, OPL outer plexiform layer, ONL outer nuclear layer, PRL photoreceptor layer. Scale bars: (a, b) 60 µm; (c, d) 10 µm.

Panx2 ablation regulates vision processes and structural components of the lens.

A comparison of the transcriptomes of 6 dpf *Panx2*$^{+/+}$ and *Panx2*$^{-/-}$ larvae identified 5355 differentially expressed genes (DEG) when the adjusted P-value (padj) was <0.05. In total, 2512

genes were up-regulated, and 2843 were down-regulated (**Fig. 4a**). The Gene Ontology analyzer for RNA-seq (GOSeq 1.56.0; (20)) identified Biological Processes (BP) and Molecular Functions (MF) that were over/under-represented in the DEG data (**Fig. 4b**). Vision-related categories like *Sensory Perception of Light Stimulus (GO:0050953; 61 genes down)* or *Sensory Perception* (GO:0007600; 70 genes down) were significantly down-regulated (**Fig. 4c,d**). The GO annotations refer to the events required for an organism to receive a sensory light stimulus, convert it to a molecular signal, and recognize as well as characterize it. The most up-regulated process was the *Humoral Immune Response* representing immune responses mediated through a body fluid *(GO:0006959; 17 genes up)* (**Fig. 4e**). *The Structural Component of the Lens (GO:0005212; 38 genes down)* was the most significantly down-regulated Molecular Function. This GO annotation refers to molecules that contribute to the structural integrity of the lens (**Fig. 4f**). The most up-regulated MFs were *Endopeptidase Regulator Activity (GO:0061135)* encompassing molecules that modulate the activity of peptidases, which can control critical functions of innate and adaptive immune responses like antigen processing and presentation of immunogenic peptides.

Next, a STRING analysis with k-means clustering of the 61 differentially down-regulated genes annotated as *Sensory Perception of Light Stimulus (GO:0050953)* showed that both the retina and the lens were affected by loss of Panx2. Cluster I represented genes with essential roles in normal vision and signal transduction in the retina. Genes belonging to the retinal arrestin family (*arr3a* and *arr3b*), rhodopsin family (*rho* and *rhol*), as well as the guanylyl cyclase family (*guca1g* and *gucy2d*), were significantly down-regulated (**Fig. 4g**). Cluster II represented lens-specific proteins belonging to the two alpha- or beta/gamma groups of the crystallin super gene families, including members of the gamma-N and gamma-M subgroups. The group represented

the M-subfamily of gamma-crystallin, which is specific to fish. These genes play essential roles in the lens structure; mutations have been shown to cause cataracts.

Genes in the up-regulated category *Humoral Immune Response (GO:0006959)* (**Fig. 4g**) showed notable up-regulated genes in *Panx2*$^{-/-}$ larvae. Genes such as *si:dkey-22f5.9, c8a, c8g, c9,* are expressed in the liver. Interestingly, genes implicated in human eye diseases (*cfb*) and age-related macular degeneration (c2/*si:ch1073-280e3.1 (F1QJB3_DANRE*) were also found to be up-regulated. The significant differential expression of retina and lens genes, as well as genes implicated in human eye disorders, led to us prioritize biological processes related to vision.

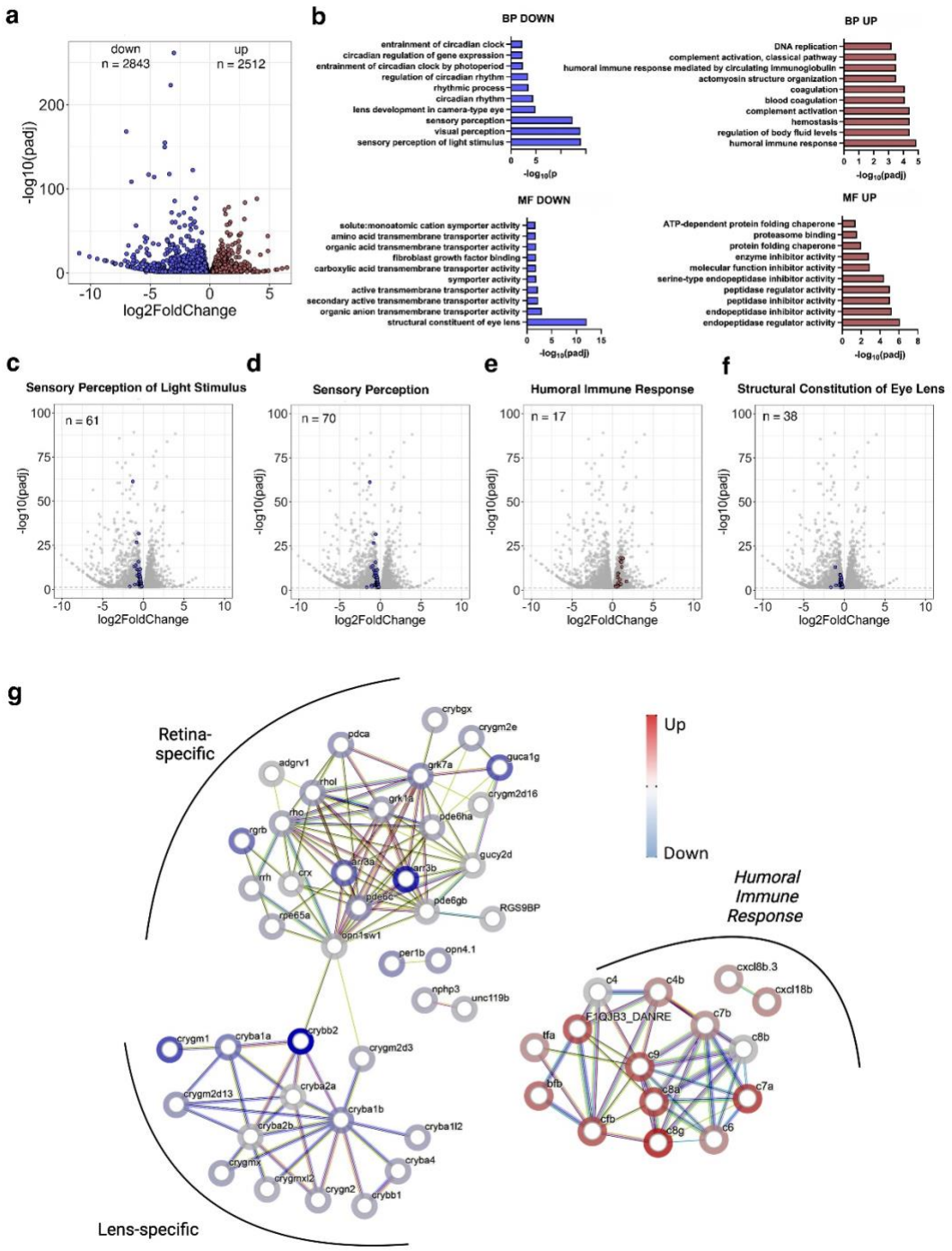

Figure 4: Panx2 ablation regulates vision processes and structural components of the lens. a) A DESeq2 analysis of RNAseq data from Panx2$^{+/+}$ and Panx2$^{-/-}$ 6dpf zebrafish larvae identified 5355 differentially expressed genes with an adjusted P-value < 0.05 b) Analysis of differentially expressed genes using GOSeq (v1.56.0). The Gene Ontology Classifier Biological Process (BP) showed significant downregulation of several vision-related categories. c,d) The most significantly down-regulated biological processes included *Sensory Perception of Light Stimulus (GO:0050953)* and *Sensory Perception (GO:0007600)***.** e) The top up-regulated BP was *Humoral*

Immune Response (GO:0006959). f) The most significantly down-regulated Molecular Function (MF) was *the Structural Component of the Lens (GO:0005212).* g) STRING analysis of 61 regulated genes annotated as *Sensory Perception of Light Stimulus (GO:0050953)* and 17 regulated genes annotated as *Humoral Immune Response (GO:0006959).* K-means clustering identified two clusters which were either retina- or lens-specific. Cluster I represents genes implicated in the phototransduction processes of the retina. Cluster II represents lens-specific proteins belonging to the alpha- or beta/gamma supergene families. A third group represents the humoral immune response.

Light-ON and light-OFF conditions affect free swimming of Panx2$^{-/-}$ larvae.

We examined visually guided behaviors to explore consequences of the differential expression of genes with roles in visual function. Baseline spontaneous swimming activity of both genotypes was analyzed at 6 dpf, during light-ON (1200 lux) and light-OFF (0 lux) phases. The representative images illustrate locomotor patterns within a single well in the light-ON condition (**Fig. 5a**). Knockout larvae preferred swimming close to the circumference of the well. In the light, *Panx2$^{-/-}$* larvae swam a shorter distance (t=7.755, df=113.1, P-value <0.001; n=24 larvae) at a lower velocity (t=7.177, df=117.6, P-value <0.001; n=24 larvae) than the *Panx2$^{+/+}$* wildtype group (**Fig. 5b,c**). In the absence of light, both *Panx2$^{+/+}$* and *Panx2$^{-/-}$* larvae exhibited a preference for the perimeter and avoided the central zone of the well (**Fig. 5d**). However, in the light-OFF condition, *Panx2$^{-/-}$* larvae swam further (t=4.147, df=88.91, P-value <0.001; n=24 larvae) at a lower steady velocity than *Panx2$^{+/+}$* larvae (t=4.095, df=96.20, P-value <0.001; n=24 larvae) (**Fig. 5e,f**).

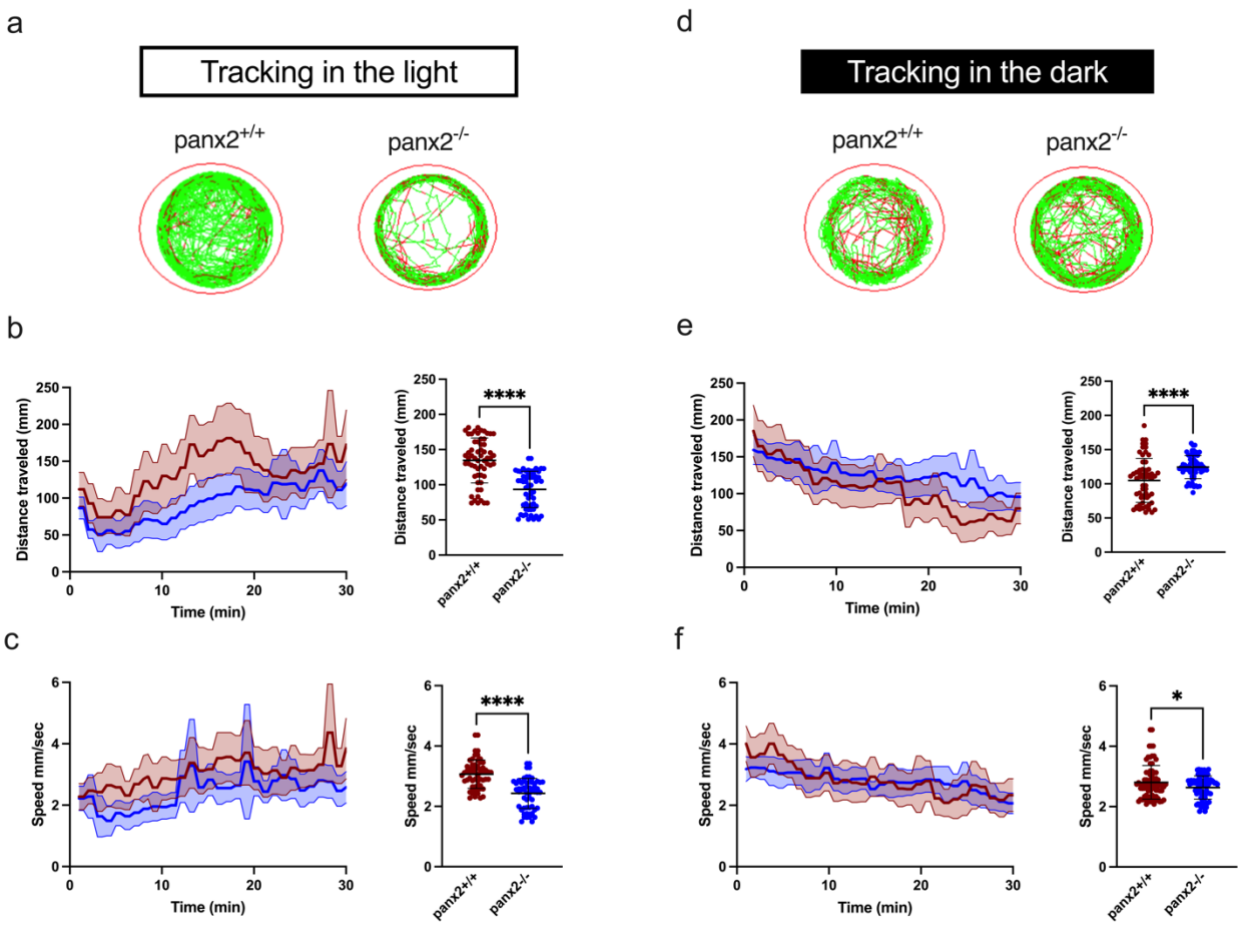

Figure 5: Light-ON and light-OFF conditions affect free swimming of *Panx2*$^{-/-}$. Representative images of a single well showing examples of *Panx2*$^{+/+}$ and *Panx2*$^{-/-}$ larvae locomotion patterns in the light (a). Medium (<20 mm/sec) or high-speed movements (>20 mm/sec) are visualized with green and red colors, respectively. Graphs demonstrate mean experimental traces ± 95% CI of distance traveled (mm) and speed (mm/sec) of 6 dpf larvae for 30 min (b,c) and their corresponding mean values, in the light. d) Representative images for each genotype, in the dark. Tracked experimental traces of distance and speed under dark conditions (e,f) and their corresponding mean ± SD. Sample sizes were n=24 larvae for each genotype. Significance: ****P-value<0.0001 and *P-value<0.05. Error bars = SD.

Panx2 ablation affects the* visual motor response *to light-ON and light-OFF stimuli.

Visual motor response (VMR) analysis was performed to compare the stereotypical motor responses of *Panx2*$^{+/+}$ and *Panx2*$^{-/-}$ larvae. The kinematic data collected provided information about seven parameters: duration of bouts, duration of bursts, freeze duration, average activity duration, bout counts, burst counts, and freeze counts. A principal component analysis identified "freeze duration" (dimension 1) and "average activity duration" (dimension 2) as capturing

73.62% and 15.14% of the data variance, respectively (**Fig. 6a**). Both parameters were selected to compare the genotypes divergence. We found that *Panx2*$^{-/-}$ larvae displayed strikingly different activity patterns for freeze duration, which represents the amount of time that the larval were immobile (**Fig. 6b**) and average activity duration (**Fig. 6c**). Panx2 knockout larvae were less active during light-ON phases, and more active in light-OFF phases. A Welch's t-test established statistical differences in mean activity of *Panx2*$^{+/+}$ and *Panx2*$^{-/-}$ in both light conditions (P-value <0.0001 for light-ON (**Fig. 6d**), P-value <0.0001 for light-OFF (**Fig. 6e**), n=24 larvae).

A modified VMR assay was performed next where the intensity of light was gradually increased; locomotor activity was measured at 10% (400 lux), 20% (800 lux) and 30% (1200 lux) light intensity. With the onset of light, *Panx2*$^{+/+}$ larvae exhibited a progressive increase in average activity duration. In contrast, *Panx2*$^{-/-}$ larvae activity was less variable as the light stimulus intensified (**Fig. 6f**). The variance analysis revealed significant differences (P-values <0.0001) in activity between *Panx2*$^{+/+}$ and *Panx2*$^{-/-}$ larvae across all levels of luminosity (**Fig. 6g,h,i**). Altogether, the differential movement responses demonstrated that *Panx2*$^{-/-}$ larvae can sense changes in light but their observed response to luminance is altered.

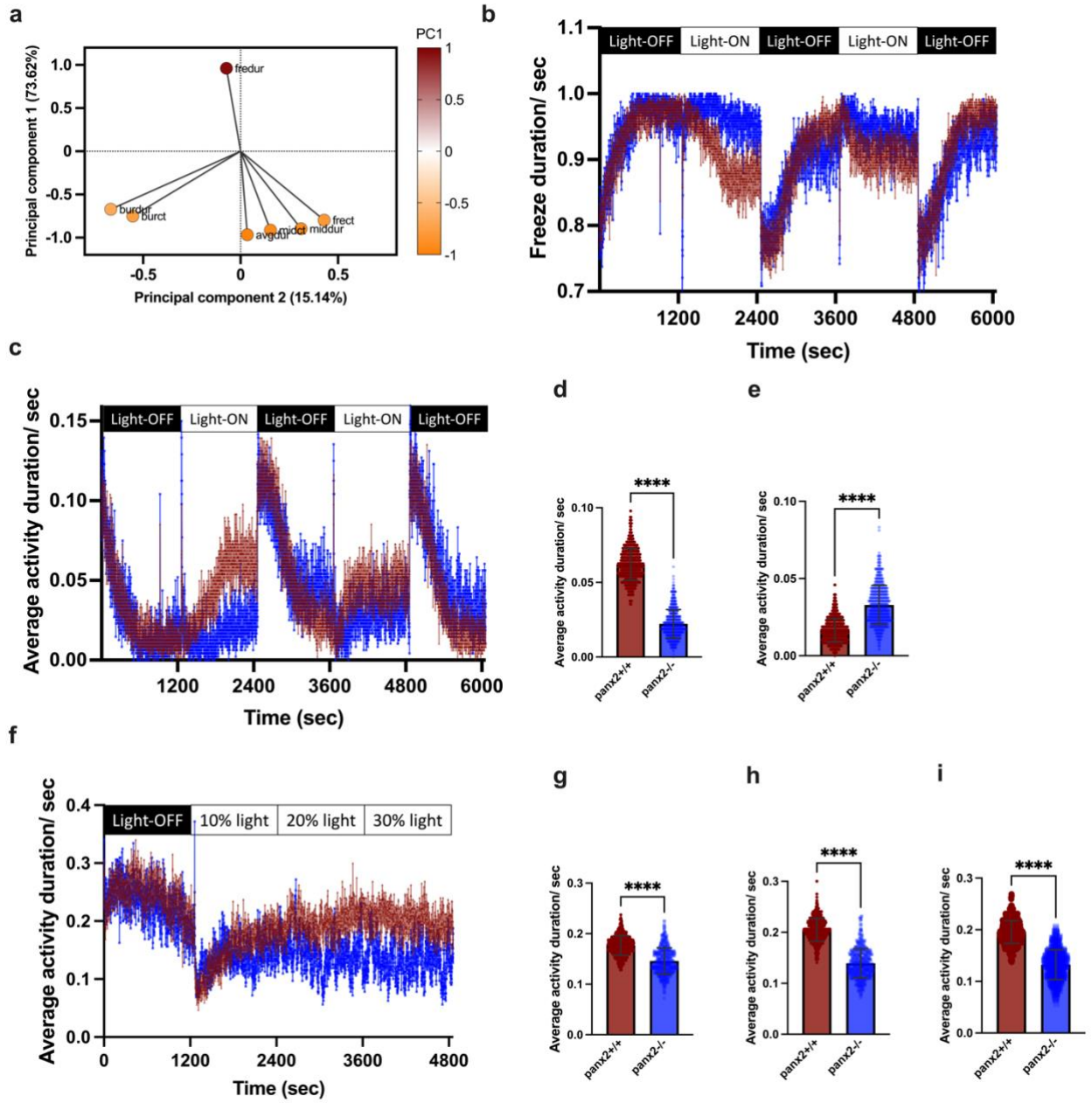

Figure 6: Panx2 ablation affects the response to light-ON and light-OFF stimuli. Principal component analysis was performed using multivariable activity data. a) The variable correlation plot indicates the coordinates of seven variables within the first two dimensions, where PC1 and PC2 capture 73.62% and 15.14% of the data variance, respectively. b) Line graph showing patterns of immobility with mean freeze duration activity for *Panx2*$^{+/+}$ (red) and *Panx2*$^{-/-}$ (blue) over alternating 20-minute periods of light-ON and light-OFF conditions. c) Line graph showing the mean average activity. Mean activity, with error bars showing SD for d) light-ON and e) light-OFF conditions, ****P-value<0.0001. f) Line graph showing the mean average activity for *Panx2*$^{+/+}$ (red) and *Panx2*$^{-/-}$ (blue) during an initial light-OFF period, followed by 20-minute increments of increasing light intensities. Mean activity, with error bars showing SD during g) 10% light intensity, h) 20% light intensity and i) 30% light intensity. ****P-value<0.0001.

GraphPad Prism was used to generate the figure and perform statistical analysis. Data shown for n=24 larvae for each genotype.

Panx2 ablation alters the optomotor response of larvae.

Optomotor response (OMR) assays evaluated the visual perception of *Panx2*$^{-/-}$ larvae. The assay enabled us to test an innate behavioral response that many animals use to stabilize themselves with respect to a visual environmental stimulus (21). Both *Panx2*$^{+/+}$ and *Panx2*$^{-/-}$ larvae responded to visual stimuli, composed of moving black and white stripes. Previously optimized parameters (22) for three spatial frequencies (SF: 64, 128, and 256 pixels/cycle), two velocities (72 and 144 pixels/sec), and two contrast levels (10% and 100%) were tested. The line graphs in **Fig. 7** summarize the percentage of positive response (PPR); corresponding to the number of larvae that showed the expected response by swimming in the direction of the stimulus (n=16 for genotype, for each distinct parameter). Altogether, *Panx2*$^{-/-}$ larvae demonstrated lower PPR and hence lower visual acuity in comparison to the wildtype group for all permutations of SF, speed, and contrast.

Under low contrast settings (10%), *Panx2*$^{-/-}$ larvae showed an average PPR of 6.94 in comparison to 45.15 for *Panx2*$^{+/+}$. The variance was most prevalent for the rightward direction at a speed of 72 pixels/sec and SF of 64, where *Panx2*$^{-/-}$ larvae did not respond while PPR for TL was 66.7 (P-value 0.00061, n=16 for each genotype). Similarly, when the stimulus was presented in the leftward direction at the same speed and SF, *Panx2*$^{-/-}$ larvae had a PPR of 8.3 in comparison to a much higher value of 58.3 for *Panx2*$^{+/+}$ (P-value 0.006, n=16 for each genotype). No statistically significant difference was observed between the two groups at the SF of 256 at 72 pixels/sec; and with the SF of 128 at 144 pixels/sec, regardless of directionality.

In the high contrast setting (100%), *Panx2*$^{-/-}$ larvae showed an average PPR of 26.38. In this luminous environment, a statistically significant difference was observed between *Panx2*$^{+/+}$ and the knockout larvae at all combinations of SF and speed. Furthermore, peak response deficiency

was observed for *Panx2*$^{-/-}$ larvae at a SF of 64; reflecting the trend seen under low contrast conditions at the same SF. While there was an increase in PPR for *Panx2*$^{+/+}$ at high contrast, when the edges of the moving stripes were well defined, there was still a considerable decrease in OMR response with the loss of Panx2. The observed decline in visual acuity of *Panx2*$^{-/-}$ larvae was found to be independent of direction (P-values: see Table 1).

Table 1: Comparison of OMR positive response percentages between *Panx2*$^{+/+}$ and *Panx2*$^{-/-}$ larvae.

		Leftward			**Rightward**		
		Spatial frequency (pixels/cycle)					
Contrast	**Speed (pixels/sec)**	**64**	**128**	**256**	**64**	**128**	**256**
Low (10%)	**72**	0.006	0.003	0.08	0.00061	0.004	0.29
	144	0.013	0.176	0.037	0.03	0.575	0.287
High (100%)	**72**	0.001	0.04	0.03	0.00061	0.03	0.001
	144	0.0014	0.036	0.012	0.0014	0.031	0.008

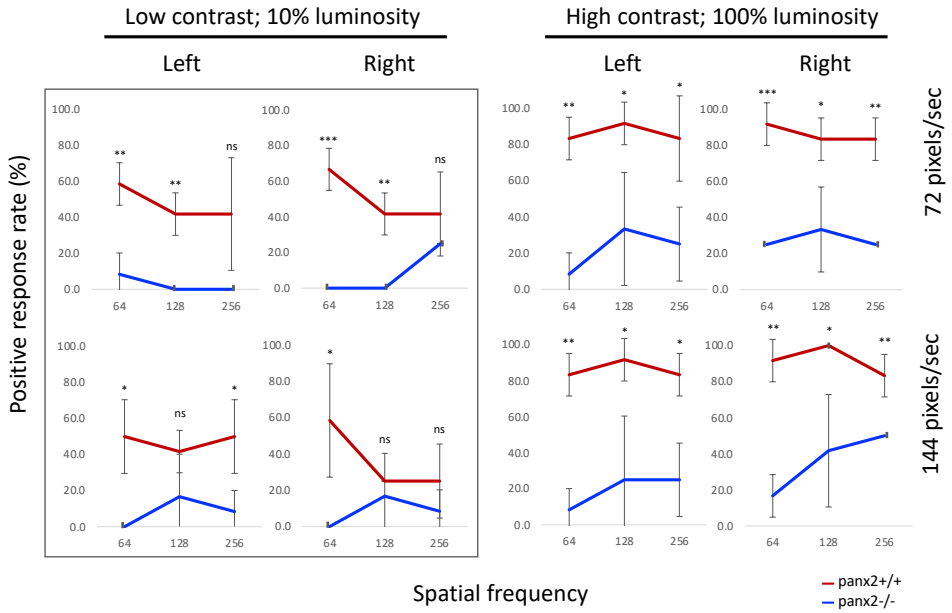

Figure 7: Optomotor response (OMR) impaired in *Panx2*$^{-/-}$ larvae. OMR was used to assess optic flow processing in 6 dpf *Panx2*$^{+/+}$ and *Panx2*$^{-/-}$ larvae, at two light intensities (10% and 100%).

Both groups were shown visual stimulus of moving stripes at three spatial frequencies (64, 128, and 256), which were presented at 72 pixels/sec and 144 pixels/sec. The line graphs show the percentage of larvae that indicated the expected positive response, from n=16 for each genotype. *Panx2*$^{-/-}$ larvae had significantly lower visual acuity when compared to *Panx2*$^{+/+}$. ***P-value<0.001, **P-value<0.01, *P-value<0.05, ns = not a significant difference.

Panx2 loss leads to lens malformation and characteristics consistent with myopia.

Whole-eye Optical Coherence Tomography (OCT) images of one-year-old *Panx2*$^{+/+}$ and *Panx2*$^{-/-}$ zebrafish were acquired using a custom-developed 1310nm Spectral Domain OCT (SD-OCT) system. An analysis of each eye was performed from a microstructural perspective and using geometric parameters, including axial length, lens diameter, retinal radius, and corneal thickness, as illustrated in **Fig. 8a**. Detailed examinations of whole-eye images revealed disruptions to the lens epithelium in *Panx2*$^{-/-}$ fish. These disruptions manifested as protruding rings within the lens, unlike the smooth, well-organized epithelium observed in *Panx2*$^{+/+}$ fish (**Fig. 8b,c,d**). We speculated that the defects could impair the lens's light-focusing ability by disrupting the normal light pathway.

The geometric data, normalized to body length, demonstrated that *Panx2*$^{-/-}$ fish had a significantly longer mean axial length (*Panx2*$^{+/+}$ = 47.57 ± 1.39 µm/mm; *Panx2*$^{-/-}$ = 51.97 ± 2.26 µm/mm; P-value <0.0001; **Fig. 8e**). Moreover, using the high-resolution whole eye OCT images we calculated the Relative Refractive Error (RRE) to investigate anomalies in refractive properties. RRE is a widely used standardized metric calculated as 1- (retinal radius/F), where F is an idealized focal length equal to lens radius × 2.324. Examination of calculated RREs revealed that Panx2 ablation led to a decrease in RRE values (*Panx2*$^{+/+}$ = 0.02 ± 0.03; *Panx2*$^{-/-}$ = -0.03 ± 0.03; P-value <0.0001; **Fig. 8f**). Eyes with a distance from the lens center to the retinal pigment epithelium (RPE) greater than the expected retinal radius exhibit negative RRE values, indicating myopic shifts. Conversely, eyes with a shorter distance (RPE closer to the lens) have positive RRE values, signifying hyperopic shifts (23). The observed statistically significant reduction of

RRE suggested myopia-like abnormalities in *Panx2*$^{-/-}$ fish. Finally, we detected an increase in corneal thickness in *Panx2*$^{-/-}$ fish, when normalized to lens diameter (*Panx2*$^{+/+}$ = 0.07 ± 0.01 µm/mm, n=38 eyes; *Panx2*$^{-/-}$ = 0.08 ± 0.01 µm/mm, n=40 eyes; P-value <0.001; **Fig. 8g,h**). For the above-mentioned parameters, we examined a total of 38 eyes from 19 *Panx2*$^{+/+}$ control and 40 eyes from 20 *Panx2*$^{-/-}$ age-matched adult fish. Altogether, our analysis demonstrated lens abnormalities in *Panx2*$^{-/-}$ fish, which suggested that Panx2 loss-of-function may contribute to myopic vision deficits in adult zebrafish.

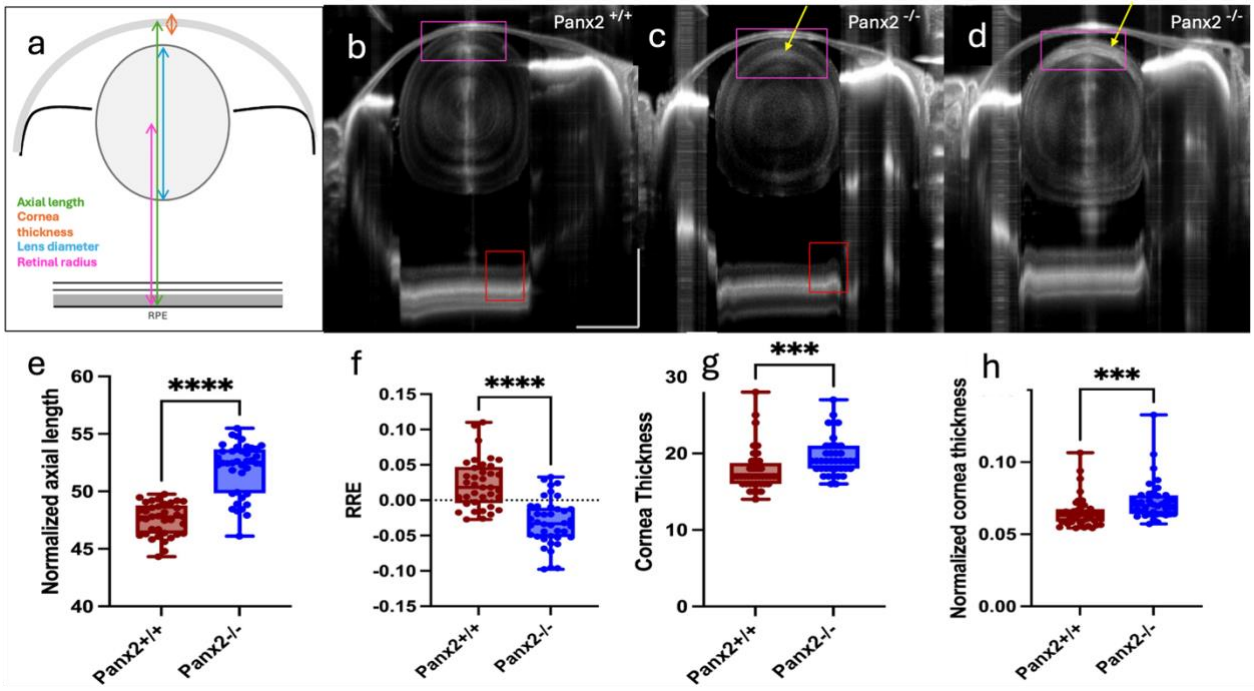

Figure 8: Loss of Panx2 leads to lens defects. Eyes of adult fish were imaged using a SD-OCT system. a) Schematic definition of four geometric parameters used for quantification of high-resolution OCT Whole-eye images. Representative images of *Panx2*$^{+/+}$ (b) and *Panx2*$^{-/-}$ (c,d), showing disruptions in lens epithelium. Scale bars = 500 µm. Bar plots showing spread of quantified geometrical parameters for the axial length normalized to body length (e), relative refractive error (f), corneal thickness (g), and corneal thickness normalized to lens diameter (h), collectively showing significant differences between the genotypes. Sample sizes for *Panx2*$^{+/+}$ and *Panx2*$^{-/-}$ were 38 and 40 eyes from 19 and 20 fish, respectively. Significance: ***P-value <0.001 and ****P-value <0.0001.

Discussion

This study demonstrates roles of Panx2 for visual function in zebrafish. We provide three lines of evidence. RNAseq data show the differential expression of genes with biological functions in the sensory perception of light. The testing of behavior in response to different light stimuli demonstrates that Panx2-deficient larvae exhibit both altered locomotor behavior in response to illumination and impaired optomotor responses, indicating defects in both visual perception and acuity. Finally, in old zebrafish, loss of Panx2 is correlated with changes to the geometry and refractive properties of eyes.

The novel results advance our previous work on pannexin functions in the visual system. We had shown previously functions of two other pannexin family members. Panx1a is predominantly expressed in the outer retina and functions in light decrement detection (24,25). Our work on Panx1b had revealed that the isoform is localized to the inner retina and ganglion cell layer (22,26). We also showed that Panx1b is expressed in the end-feet of Muller glial cells which was first evidence for a unique cell type specific expression, - neuronal versus glial -, that is unique to fish (22). Behavioral analyses have revealed distinct phenotypes for Panx1a and Panx1b knockout zebrafish. Panx1a KOs exhibited altered visual motor responses (VMR), characterized by a general reduction in activity and specific deficits in dark phase locomotion (25). Panx1b knock outs, on the other hand, showed impairments in optic flow direction-selectivity, particularly at high spatiotemporal frequencies and low contrast surroundings (22). It was also demonstrated that Panx1a and Panx1b function in the outer retina as the slow negative feedback signal from HCs to cones to generate the center/surround organization of bipolar cell receptive fields (27). Here, we show that Panx2 is expressed in both the inner and outer retinal layers, with prominent expression in the photoreceptor inner segment. Our data aligns with a previous report, in the murine model, which showed that Panx2 is expressed in the photoreceptor

inner segment and outer plexiform layer of the mouse retina (7). Panx2 KO larvae exhibit a pronounced reduction in locomotor activity during light phases and an increase in locomotor activity during dark phases, a pattern that is markedly different from the VMR phenotypes observed in Panx1a/b KOs (22,25). Furthermore, the OMR response in Panx2 KOs is severely impaired during both low and high contrast conditions, regardless of direction. Thus, our findings for Panx2 KO larvae suggest a severe and distinct role in retinal function compared to Panx1a/b. Consistent with the behavioral data, RNAseq analysis identified a marked decrease in the expression of genes involved in the detection of light stimuli in Panx2 knockouts. We speculate that Panx2 plays a critical role in retinal signaling that is not redundant with Panx1a or Panx1b. It is likely that their specific functions may be complementary or synergistic, contributing to different aspects of visual processing.

The observed expression patterns and widespread changes in gene expression and behaviour highlight a pivotal role of Panx2 in retinal physiology. Its strategic localization at ER-mitochondria contacts (MAMs) and its abundance in the neuropil, a critical region for synaptic transmission, suggest that the neuronal deficits in Panx2 knockout fish could stem from disruptions in bioenergetics and synaptic function. Given their highly compartmentalized nature, neurons rely on precise calcium control, which is essential for their function. The endoplasmic reticulum (ER) and mitochondria are critical for this regulation (28). Mitochondria, in addition to providing energy to postsynaptic spines, also help maintain calcium homeostasis (29). We reason that the loss of Panx2 function in the inner segments of photoreceptors affects the biosynthetic machinery essential for photoreceptor function. Inner segments are rich in mitochondria, and together with mitochondria-associated membranes (MAMs) play a crucial role as contact sites between the endoplasmic reticulum (ER) and mitochondria, facilitating the transfer of calcium and other signals. Studies indicate that

dysfunction in the inner segment's ability to produce energy can lead to vision loss and degenerative diseases like retinitis pigmentosa and age-related macular degeneration (30). Additionally, disruptions in the inner segment's metabolic processes are associated with stress responses that may lead to photoreceptor cell death, impacting vision over time (31). The intricate network of ER-mitochondria connections, as revealed by recent imaging techniques, underscores the importance of MAMs in regulating calcium concentrations and energy dynamics within neurons (17). We know that the metabolic demands of synaptic transmission are substantial, requiring a constant supply of ATP (32). It is possible then that Panx2-mediated processes within the ER-mitochondrial axis influence energy production or utilization, leading to deficits in neuronal function. Additionally, the enriched expression of Panx2 in the neuropil suggests its involvement in regulating synaptic transmission, potentially through its role in calcium signaling or mitochondrial dynamics, which are known to influence the efficiency of energy production. Studies have shown that ER releases calcium in dendrites upon synaptic stimulation, which is subsequently buffered by mitochondria. Moreover, the tethering of mitochondria to the ER might influence the duration of ER residence in spines, potentially affecting synaptic plasticity (33). Computational modeling has further emphasized the role of MAMs in regulating calcium and ATP dynamics within neurons, highlighting the importance of MAMs communication in shaping synaptic signaling (28). Interestingly, prior overexpression studies revealed that both paralogs of Panx2, Panx1 and Panx3, can form calcium-permeable ER channels (34,35). These possibilities allude to the role of Panx2 in supporting retinal function; and indicate that its influence likely extends beyond the visual signaling pathway.

Both Panx1 and Panx2 expression has been identified previously in the adult murine lens epithelium (36). In adult zebrafish, Panx2 ablation resulted in lens malformations consistent with myopia. RNA-seq data collaborated this finding, indicating differential expression of genes

associated with the structural components of the eye lens early in life. Significantly downregulated genes were those for lens-specific proteins, including alpha- and beta/gamma-crystallins, as well as fish-specific M-subfamily gamma-crystallins. These genes are essential for maintaining lens structure, and mutations in them can lead to cataracts (37,38). These results reinforce the possibility that Panx2 is critical for cellular energy homeostasis. The loss of Panx2 could disrupt the energy supply to lens cells, hindering their growth and differentiation and hence potentially resulting in a myopic phenotype. Additionally, cellular stress induced by metabolic disruptions may contribute to the development of myopia-related ocular changes, such as altered lens curvature or axial elongation. Collectively, our study underscores the multifaceted role of Panx2 in retinal physiology.

Beyond its impact on vision, transcriptome profiling also suggested that Panx2 is a novel regulator of immune responses, with immune activation potentially exacerbating retinal and lens degeneration in aged animals. While we have not prioritized investigating this result it implies that Panx2 plays multifaceted roles in maintaining visual acuity, regulating ocular morphology, and moderating neuro-immune interactions crucial for retinal and lens development and health. In this regard this study's implications extend to understanding the neuro-immune axis in vision and suggest that Panx2 could be a therapeutic target for conditions involving retinal degeneration, immune dysregulation, cataracts, or myopia.

Materials and Methods

Zebrafish lines.

Zebrafish (*Danio Rerio*) of strain Tubingen long fin (TL) were maintained in groups with mixed sex in a recirculation system (Aquaneering Inc., San Diego, CA) at 28ºC on a 14hr light/10hr dark cycle. All animal work was performed at York University's zebrafish vivarium and in an S2 biosafety laboratory following the Canadian Council for Animal Care guidelines after approval of the study protocol by the York University Animal Care Committee (GZ#2019-7-R2).

Generating *Panx2*$^{-/-}$ zebrafish.

Potential TALENs target sites were identified using Mojo Hand software (http://talendesign.org) (11,12). TALENs targeted exon 1 of the *panx2* gene (NM_001256641). The TALEN constructs were synthesized in Dr. Stephen Ekker's lab (Mayo Clinic Cancer Center, Rochester, MN). TALEN assemblies of the repeat-variable di-residues (RVD-containing repeats) were conducted using the Golden Gate approach (39). pT3TS-GoldyTALEN expression vectors (40,41). Plasmids were linearized with the SacI restriction endonuclease (ThermoFisher Scientific, Canada) for 15 min at 37°C and used as templates for *in vitro* transcription.

Capped cRNAs were synthesized from TALEN pairs mixed 1:1 using the mMESSAGE mMACHINE T3 Transcription kit (Life Technologies, Canada) and purified using the Oligotex mRNA Mini Kit (Qiagen Inc., Toronto, Canada). TALEN cRNAs were diluted in DNase/RNase-free water (Life Technologies) to the final concentration of 1 µg/µL and stored at −80 °C before microinjection.

One-cell stage zebrafish embryos were microinjected with TALEN cRNAs pair at a dose of 25 pg/nl. Genomic DNA (gDNA) was extracted from injected embryos at 4 dpf to examine the TALEN mutagenesis efficiency. Individual larvae were incubated in 100 mM NaOH at 95℃ for 15 min. After cooling to room temperature, one-tenth of the 1 M Tris (pH8.0) volume was added to the extracts to neutralize the NaOH. Finally, 1 volume TE buffer pH 8.0 was added, and gDNAs were stored at -20℃. gPCR was used as a screen to detect small indel mutations by BamHI restriction enzyme (RE) digests. PCR primers for genotyping: 5'-CGAATGCAGAATATCCTCGAGCAG-3'; reverse, 5'-GTGACGACCCGGTCAAAGG-3'. Indel mutations were confirmed by sequencing (Eurofins Genomics LLC, KY, USA) of gel-purified PCR products cloned into the pJet1.2 cloning vector (Life Technologies).

Adult mosaic zebrafish (F0) were anesthetized in pH-buffered ethyl 3-aminobenzoate methanesulfonate solution (0.2 mg/ml; MS-222, Sigma-Aldrich). A section of the caudal fin was removed using dissecting scissors (WPI Inc., FL, USA) and placed into 1.5 ml collecting tubes. The fin gDNA was isolated and screened for indel mutations as described (40). Adult F0 zebrafish were out-crossed to wild-type (WT) TL zebrafish and their F1 offspring were analyzed by PCR and *BamHI* restriction digestions to verify germline transmission of mutations. Heterozygous *Panx2*$^{+/-}$ F1 mutants were in-crossed to establish homozygous F2 mutants *Panx2*$^{-/-}$. All experiments described were performed with progenies of F3 or alter generations. Age matched siblings served as controls.

NGS RNA-sequencing.

The transcriptomes of the *Panx2*$^{-/-}$ and sibling controls (*Panx2*$^{+/+}$) were analyzed by RNA-seq (NGS-Facility, The Center for Applied Genomics, SickKids, Toronto, ON, Canada). The raw data represented the sequencing of three independent pools of ≈30 age-matched larvae at 6 dpf. The RNA-seq data are deposited at the NCBI - Gene Expression Omnibus (GEO) database repository (ID pending). Total RNAs were extracted using RNeasy Plus Mini Kit (Qiagen). The RNA quality was determined using a Bioanalyzer 2100 DNA High Sensitivity chip (Agilent Technologies, Mississauga, ON, Canada). The RNA library preparation was performed following the NEB NEBNext Ultra II Directional RNA Library Preparation protocol (New England Biolabs Inc., Ipswich, MA, USA). RNA libraries were loaded on a Bioanalyzer 2100 DNA High Sensitivity chip to check for size, quantified by qPCR using the Kapa Library Quantification Illumina/ABI Prism Kit protocol (KAPA Biosystems, Wilmington, MA, USA). Pooled libraries were paired-end sequenced on a High Throughput Run Mode flow cell with the V4 sequencing chemistry on an Illumina HiSeq 2500 platform (Illumina, Inc., San Diego, CA) following Illumina's recommended protocol to generate paired-end reads of 126-bases in length.

Differential Gene Expression and Functional Enrichment Analyses.

The post-sequencing processing to final read counts, normalization, and differential gene expression analysis used multiple software packages, including a two-condition differential expression analysis using the edgeR R-package, v.4.0.16 (42,43) and DESeq2 R package version 1.42.1 (44). Genotypes were incorporated into the statistical model and multiple hypothesis testing was performed. The default filter for DESeq2 used a threshold of $p<0.05$ and the Benjamini-Hochberg procedure to determine the false discovery rate (FDR), and the adjusted P-value (padj).

A Gene Set Enrichment Analysis (GSEA) tested whether a defined set of genes shows statistically significant, concordant differences between genotypes. The data were filtered at padj < 0.05 and analyzed for enrichment using R GOseq (v1.56.0) (20). Other tools used to process RNA-seq data were HCOP (https://www.genenames.org/tools/hcop/) and db2db at bioDBnet (https://biodbnet.abcc.ncifcrf.gov/db/db2db.php) to convert curated human or mouse to zebrafish genes (45,46). Curated gene lists were generated based on GOseq and analyzed in STRING v12.0 (string-db.org) (47). The top-scoring categories were visualized using ggplot2 (v3.5.1) from the tidyverse package (v2.0.0) in R (48).

Hybridization chain reaction RNA-fluorescence in situ hybridization (HCR RNA-FISH). Larvae were raised under standard conditions in egg water. When embryos reached 12 hours post-fertilization (hpf), egg water was replaced with egg water containing 0.003% of 1-phenyl 2-thiourea (PTU). Fresh egg water containing 0.003% PTU was replaced every 24 hours until the larvae reached 5 dpf. At 6 dpf, the larvae were euthanized and fixed in 4% ice-cold paraformaldehyde (PFA). After 24 hours, the PFA was washed out with 1× PBS, and the samples were gradually dehydrated, permeabilized with methanol, and stored at −20 °C for several days until HCR in situ labelling was performed.

Staining was performed according to the manufacturer's protocol for whole-mount zebrafish larvae (49). Specifically, the samples were separated into 5 larvae per well in a 24-well plate. Rehydration steps were performed by washing for 5 minutes each in 75% methanol/PBST (1× PBS + 0.1% Tween-20), 50% methanol/PBST, 25% methanol/PBST, and 5 times with 100% PBST. The samples were permeabilized with 30 µg/ml proteinase K for 45 minutes at room temperature, followed by post-fixation with 4% PFA for 20 minutes at room temperature, and five washes in PBST for 5 minutes each. The samples were prehybridized in 500 µl of probe hybridization buffer (Molecular Instruments) for 30 minutes at 37 °C. Hybridization was performed by adding 2 pmol of each probe set to the hybridization buffer and incubating for 16 hours at 37 °C. Probe sets for *panx2* were purchased from and designed by Molecular Instruments using proprietary HCR methodology to detect and fluorescently label target RNA transcripts. To maximize targeting, the probe was designed against shared regions of known variants found on NCBI Gene and the Ensembl database. Each probe set consisted of 20 split-initiator probe pairs per target and utilized a B1 amplifier with a 546 nm fluorophore label. To remove excess probes, the samples were washed 4 times for 15 minutes each with a wash buffer (Molecular Instruments) at 37 °C, followed by 2 washes of 5 minutes each with 5× SSCT (5× SSC + 0.1% Tween-20) at room temperature. Pre-amplification was performed by incubating the samples for 30 minutes in an amplification buffer (Molecular Instruments) at room temperature. The fluorescently labelled hairpins (B2-488) were prepared by snap cooling: heating at 95 °C for 90 seconds and then cooling to room temperature for 30 minutes. The hairpin solution was prepared by adding 10 µl of the snap-cooled hairpins (3 µM stock concentration) to 500 µl of amplification buffer. The pre-amplification buffer was removed, and the samples were incubated in the hairpin solution for 16 hours at room temperature. Excess hairpins were washed three times with 5× SSCT for 20 minutes each. Following HCR RNA-FISH, larvae were stained with DAPI (1:12,000) overnight

at 4 °C, followed by three 10-minute washes in 5× SSCT. The samples were then stored in 5× SSCT in the dark at 4 °C until imaging.

A z-mold or an 8-teeth mold for zebrafish larvae was 3D-printed using 2% low melting agarose on glass-bottom culture dishes (MatTek, P35G-0-10C) (50). The larvae were positioned in larva-shaped slots and embedded dorsal side down in 0.5% low melting agarose. Images were acquired on the Nikon A1R confocal system with either a 20XW or 40XO objective using the 546 nm (B1 amplifier) and 468 nm lasers. Image analysis was performed using ImageJ (v2.9.0).

Quantitative real-time PCR (qRT-PCR) analysis.

Total RNA (1 µg) was extracted and purified from pools of 30 zebrafish larvae at 6 dpf using the RNeasy Plus Mini Kit (Qiagen, Germantown, MD, United States of America) as per the manufacturer's protocols. Fish were homogenized by bead beating in 1xTE buffer (pH 8.0). RNAs were reverse transcribed into cDNA using the iScript Reverse Transcription Supermix (Bio-Rad, Mississauga, ON, Canada) as per the manufacturer's instructions. Gene expression was analyzed by qRT-PCR using the SsoAdvanced universal SYBR Green Supermix (Bio-Rad, Mississauga, ON, Canada) in the CFX96™ Real-Time PCR Detection System (Bio-Rad, Mississauga, ON, Canada). Thermal cycling was carried out for 39 cycles of the following: 94°C for 30 s, 50°C for 30 s, and 72°C for 1 min. The housekeeping gene, *18S*, was used to determine the quality of the samples and for normalization purposes. CT values were averaged and exported from the CFX Manager Software (Bio-Rad, Mississauga, ON, Canada). The fold-difference for the relative gene expression was calculated in the Relative Expression Software Tool VS. 2009 (Pfaffl et al., 2002). Three technical replicates per gene were performed from three biological replicates.

Immunohistochemistry.

Larvae (6 dpf) were humanely euthanized in MS-222 solution (0.02% w/v, Sigma-Aldrich) and fixed in 4% paraformaldehyde (PFA) in 1xPBS overnight at 4ºC, followed by cryoprotection in 30% sucrose in 1xPBS. After embedding in Tissue-Tek O.C.T compound 15µm sections were cut on a cryotome (Thermofisher). Samples were washed three times for 5 min with 1xPBS containing 0.1% Tween-20 (PBST) at RT. Unspecific binding sites were blocked with freshly prepared 5% normal goat serum (NGS, Sigma-Aldrich) in PBST for 1hr at RT℃. Following blocking, samples were incubated with a custom-made primary rabbit anti-Panx2 antibody (1:200, catalog #A01856, GenScript) overnight at 4°C. Subsequent washes with PBST were for one hour at 4 ℃. The Alexa 488 goat anti-rabbit secondary antibody (1:20,000 in 1% NGS PBST,

catalog#A11034, Life Technologies) was applied for one hr at RT. After 3 washes with PBST followed by one wash with water, specimens were mounted on microscope slides using ProLong Antifade with DAPI (Thermofisher). Confocal images were collected using LSM-ZEN2 software (Zeiss LSM700 system; Carl Zeiss MicroImaging, Oberkochen, Germany) with Plan-Apochromat 20x/0.8 or Plan-Apochromat 63x/1.3 oil DIC M27 objectives. For comparison of wild type and knockout tissues settings for raw image collection were identical. Post image collection composite figures were created using Adobe Photoshop 2021.

Zebrafish Locomotion Assays.

The Zebrabox behavior system and the ZebraLab analytical suite (ViewPoint Life Technology, Lyon, France, http://www.viewpoint.fr) were used for automated extraction of behavioral outputs and video tracking. Tracking videos were recorded at 30 frames per second (fps) under infrared (for light-OFF recording) or visible light (light-ON) illumination using a Point Grey Research Dragonfly2 DR2-HIBW camera (Teledyne-FLIR, Burlington, ON, Canada). Inside the Zebrabox a lightbox provided visible and infrared light from below for recordings using 0% to 30% light intensity (visible range, 0-1200 lux). 6 dpf larvae were observed in 24 or 48-well plates maintained at 28ºC throughout the experiment. All experiments were performed between 12:00 to 2 pm, as larvae (6 dpf) activity was previously reported to reach a stable level by early afternoon.

Spontaneous free-swimming assay.

Larval swimming activity under constant light-ON/OFF conditions was tested using 24-well plates. Locomotor behavior was tracked for 30 min. For analysis of locomotion, three thresholds were defined: slow (<2mm), medium (2-20mm), and fast (>20mm). The mean total distance traveled (mm) and velocity (mm/sec) in two swim speeds *(medium and fast)* were used for statistical analysis.

Visual Motor Response (VMR) assay.

Zebrafish larvae (n=24 per genotype) were acclimatized to darkness for 2 hours in a 48-well plate. Baseline activity was recorded for 21 minutes under light-OFF conditions. For the first experiment, larvae were subjected to alternating 20-minute light-on (30%, 1200 lux) and light-off periods, totaling 1 hour and 41 minutes. For the second experiment, a modified protocol involved incremental 10% light intensity increases every 20 minutes, culminating in 30% (1200 lux) light intensity after 1 hour and 21 minutes. Data acquisition for all experiments was conducted using the Quantization® mode of Zebrabox. Data collected at each time point included freeze count,

freeze duration, mid count, mid duration, burst count, and burst duration. For analysis, the average duration (mean of mid and burst durations) was calculated for each larva.

Opto Motor Response (OMR).

OMR assays were performed using a custom-built system, which follows the design described (Stih, Petrucco et al. 2019). Briefly, stimuli were presented from below using an ASUS P3B 800-Lumen LED portable projector (https://www.asus.com/ca-en/Projectors/P3B/). The fish movements were recorded using a USB 3.1 high-speed camera (XIMEA GmbH, Germany) equipped with a 35mm C Series Fixed Focal Length Lens (Edmund Optics Inc., USA). An 830 nm long-pass filter (Edmund Optics Inc., USA) was used to block infrared illumination coming from a source at the bottom of the test environment. The videos were recorded using the XIMEA Windows Software Package (https://www.ximea.com/support/wiki/apis/XI-MEA_Windows_Software_Package). Visual stimuli were generated with an online stimulus generator program called "Moving Grating" (available at https://michaelbach.de/sci/stim/movingGrating/index.html).

During experiments four larvae in a 3 cm dish (Thermo Scientific) were allowed to acclimatize for 5 min before starting the video recording. The visual stimulus consisted of sequences of alternating white and black stripes generated with 64/128/256 pixels/cycle spatial frequency. The speed rate was set to 72/144 pixels/sec. The contrast was set to 10%, where the stripes appeared as white and grey, or 100%, where the stripes appeared as white and black. Stimuli were presented to larvae (n = 4, for each of the four independent experimental repeats) for 30 seconds in the left or right direction. Once the larvae oriented towards the moving stimulus and initiated a sustained swimming motion in the direction of the stimulus, it was counted as a positive response. The positive rate of response was used for analysis. This value was expressed as a percentage: number of larvae that swam in the direction of the stimulus/ total number of larvae in the dish.

Optical coherence tomography (OCT) assay.

A custom-developed spectral-domain optical coherence tomography (SD-OCT) system was built in a Michelson configuration, employing a super luminescent laser diode centered at 1,310 nm (± 75 nm at 10 dB; Exalos, Switzerland) and a 2048-pixel line scan camera spectrometer with a maximum acquisition rate of 147kHz (Wasatch Photonics; United States of America). A 50/50 fiber coupler splits the source light into the reference and sample arms. In the sample arm, the output light illuminates the sample surface after passing through a reflective beam collimator

(Thorlabs; United States of America), a 2-DOF galvo mirror, and an objective lens (LSM02, Thorlabs; United States of America). The 2-DOF Galvo mirror allows for collection of reflected light from the sample while raster scanning sample surface. In the reference arm, a polarization controller, a dispersion compensation block, and a gold-coated reference mirror were installed. The back- reflected light of these two arms is subsequently merged after passing through the beam splitter and redirected to the spectrometer by the optical circulator. The formed interference pattern in the spectrometer is captured by a line scan camera. The captured signal is digitized and sent to the computer for processing. To form an A-line (i.e., depth profile of sample reflections at a given point on sample surface), the tomograms of the sample is background subtracted and mapped to k-space before applying Fourier transformation to calculate depth profile of reflectors in the z-space (physical depth space). Processes were repeated for data acquired during raster scanning of beam on sample surface to eventually form 3-D OCT volumetric images of zebrafish eye. The axial and lateral resolutions of the system in tissue were measured as 8.5 μm and 10 μm, respectively. Before imaging, age-matched adult zebrafish were humanely euthanized using MS222. Fish were then placed in a silicon mold to orient the eye toward OCT system's objective lens. To minimize specular reflections from sample surface, a thin layer of PBS (~80 μm) was placed over the eye before imaging. All captured OCT images were calibrated for image pixel size in axial and lateral directions before interrogation in ImageJ software and quantification of the geometrical parameters.

Statistics and data reproducibility.

Statistical analyses were performed in GraphPad Prism VS10.2.3. Results are represented as the mean ± standard deviation (SD) or standard error of the mean (SEM) for behavioural data. For molecular analysis (RT-qPCR, RNA-seq), a minimum of $n \geq 3$ independent experimental replicates were generated. For behavioral testing G*power analysis determined the number of larvae. The normality and homogeneity of the data variance were determined by the "Shapiro-Wilk Test" and "Levene's Test." Experimental groups were compared using unpaired t-tests or Welch's t-tests. A P value <0.05 was considered statistically significant. For all experiments, sample sizes, statistical tests, and when appropriate P-values are indicated in the figure legends.

Acknowledgements

We thank two members of York University Zebrafish Vivarium, Janet Fleites-Medina, and Veronica Scavo for outstanding zebrafish husbandry. We also wish to thank the Center for Applied Genomics, SickKids, Toronto, ON, Canada for the RNA-seq service.

Funding

This research was supported by the Natural Sciences and Engineering Research Council (NSERC) discovery grant RGPIN-2019-06378 (GRZ).

Author contributions

Conceptualization, RS, GRZ; data analysis, RS, GSZ, FN, SS, AB; investigation, all authors; writing – original draft preparation, RS, GRZ; writing – review and editing, all authors; visualization, RS, GSZ, FN, SS, AB; supervision, NT, GRZ; project administration, GRZ; funding acquisition, GRZ.

Consent for publication

All authors have read and agreed to the published version of the manuscript.

Ethics approval

All animal work was performed at York University's zebrafish vivarium and in an S2 biosafety laboratory following the Canadian Council for Animal Care guidelines after approval of the study protocol by the York University Animal Care Committee (GZ#2019-7-R2).

Data Availability

The RNA-seq data are deposited at the NCBI - Gene Expression Omnibus (GEO) database repository (ID pending at time of submission). Additional information necessary for the reanalysis of the data reported in this manuscript is available from the corresponding author upon request.

Competing interests

The authors declare no competing interests.

Materials & Correspondence

Correspondence and material requests should be addressed to Riya Shanbhag, Georg R. Zoidl.

References

1. Panchina Y, Kelmanson I, Matz M, Lukyanov K, Usman N, Lukyanov S. A ubiquitous family of putative gap junction molecules. Current Biology. 2000 Jun 1;10(13):R473–4.

2. Vogt A, Hormuzdi SG, Monyer H. Pannexin1 and Pannexin2 expression in the developing and mature rat brain. Molecular Brain Research. 2005 Nov 18;141(1):113–20.

3. Swayne LA, Sorbara CD, Bennett SAL. Pannexin 2 is expressed by postnatal hippocampal neural progenitors and modulates neuronal commitment. J Biol Chem. 2010 Aug 6;285(32):24977–86.

4. Baranova A, Ivanov D, Petrash N, Pestova A, Skoblov M, Kelmanson I, et al. The mammalian pannexin family is homologous to the invertebrate innexin gap junction proteins. Genomics. 2004 Apr 1;83(4):706–16.

5. Bond SR, Wang N, Leybaert L, Naus CC. Pannexin 1 Ohnologs in the Teleost Lineage. J Membrane Biol. 2012 Aug 1;245(8):483–93.

6. Zoidl G, Kremer M, Zoidl C, Bunse S, Dermietzel R. Molecular diversity of connexin and pannexin genes in the retina of the zebrafish Danio rerio. Cell Commun Adhes. 2008 May;15(1):169–83.

7. Le Vasseur M, Lelowski J, Bechberger JF, Sin WC, Naus CC. Pannexin 2 protein expression is not restricted to the CNS. Frontiers in Cellular Neuroscience [Internet]. 2014 [cited 2024 Feb 21];8. Available from: https://www.frontiersin.org/articles/10.3389/fncel.2014.00392

8. He Z, Zhao Y, Rau MJ, Fitzpatrick JAJ, Sah R, Hu H, et al. Structural and functional analysis of human pannexin 2 channel. Nat Commun. 2023 Mar 27;14(1):1712.

9. Zhang H, Wang S, Zhang Z, Hou M, Du C, Zhao Z, et al. Cryo-EM structure of human heptameric pannexin 2 channel. Nat Commun. 2023 Mar 3;14(1):1118.

10. Sanchez-Pupo RE, Johnston D, Penuela S. N-Glycosylation Regulates Pannexin 2 Localization but Is Not Required for Interacting with Pannexin 1. Int J Mol Sci. 2018 Jun 22;19(7):1837.

11. Ambrosi C, Gassmann O, Pranskevich JN, Boassa D, Smock A, Wang J, et al. Pannexin1 and Pannexin2 channels show quaternary similarities to connexons and different oligomerization numbers from each other. J Biol Chem. 2010 Aug 6;285(32):24420–31.

12. Penuela S, Bhalla R, Nag K, Laird DW. Glycosylation Regulates Pannexin Intermixing and Cellular Localization. Mol Biol Cell. 2009 Oct 15;20(20):4313–23.

13. Boassa D, Nguyen P, Hu J, Ellisman MH, Sosinsky GE. Pannexin2 oligomers localize in the membranes of endosomal vesicles in mammalian cells while Pannexin1 channels traffic to the plasma membrane. Front Cell Neurosci. 2014;8:468.

14. Wicki-Stordeur LE, Boyce AKJ, Swayne LA. Analysis of a pannexin 2-pannexin 1 chimeric protein supports divergent roles for pannexin C-termini in cellular localization. Cell Commun Adhes. 2013 Aug;20(3–4):73–9.

15. Le Vasseur M, Chen VC, Huang K, Vogl WA, Naus CC. Pannexin 2 Localizes at ER-Mitochondria Contact Sites. Cancers (Basel). 2019 Mar 11;11(3):343.

16. Wang N, Wang C, Zhao H, He Y, Lan B, Sun L, et al. The MAMs Structure and Its Role in Cell Death. Cells. 2021 Mar 16;10(3):657.

17. Lee A, Hirabayashi Y, Kwon SK, Lewis TL, Polleux F. Emerging roles of mitochondria in synaptic transmission and neurodegeneration. Curr Opin Physiol. 2018 Jun;3:82–93.

18. Markovinovic A, Greig J, Martín-Guerrero SM, Salam S, Paillusson S. Endoplasmic reticulum–mitochondria signaling in neurons and neurodegenerative diseases. Journal of Cell Science. 2022 Feb 1;135(3):jcs248534.

19. Missiroli S, Perrone M, Gafà R, Nicoli F, Bonora M, Morciano G, et al. PML at mitochondria-associated membranes governs a trimeric complex with NLRP3 and P2X7R that modulates the tumor immune microenvironment. Cell Death Differ. 2023 Feb;30(2):429–41.

20. Young MD, Wakefield MJ, Smyth GK, Oshlack A. Gene ontology analysis for RNA-seq: accounting for selection bias. Genome Biology. 2010 Feb 4;11(2):R14.

21. LeFauve MK, Rowe CJ, Crowley-Perry M, Wiegand JL, Shapiro AG, Connaughton VP. Using a variant of the optomotor response as a visual defect detection assay in zebrafish. J Biol Methods. 2021;8(1):e144.

22. Safarian N, Houshangi-Tabrizi S, Zoidl C, Zoidl GR. Panx1b Modulates the Luminance Response and Direction of Locomotion in the Zebrafish. International Journal of Molecular Sciences. 2021 Jan;22(21):11750.

23. Collery RF, Veth KN, Dubis AM, Carroll J, Link BA. Rapid, Accurate, and Non-Invasive Measurement of Zebrafish Axial Length and Other Eye Dimensions Using SD-OCT Allows Longitudinal Analysis of Myopia and Emmetropization. PLOS ONE. 2014 Oct 21;9(10):e110699.

24. Prochnow N, Hoffmann S, Vroman R, Klooster J, Bunse S, Kamermans M, et al. Pannexin1 in the outer retina of the zebrafish, Danio rerio. Neuroscience. 2009 Sep 15;162(4):1039–54.

25. Safarian N, Whyte-Fagundes P, Zoidl C, Grigull J, Zoidl G. Visuomotor deficiency in panx1a knockout zebrafish is linked to dopaminergic signaling. Sci Rep. 2020 Jun 12;10(1):9538.

26. Kurtenbach S, Prochnow N, Kurtenbach S, Klooster J, Zoidl C, Dermietzel R, et al. Pannexin1 Channel Proteins in the Zebrafish Retina Have Shared and Unique Properties. PLOS ONE. 2013 Oct 23;8(10):e77722.

27. Cenedese V, de Graaff W, Csikós T, Poovayya M, Zoidl G, Kamermans M. Pannexin 1 Is Critically Involved in Feedback from Horizontal Cells to Cones. Front Mol Neurosci. 2017;10:403.

28. Leung A, Ohadi D, Pekkurnaz G, Rangamani P. Systems modeling predicts that mitochondria ER contact sites regulate the postsynaptic energy landscape. npj Syst Biol Appl. 2021 Jun 2;7(1):1–14.

29. Tsuboi M, Hirabayashi Y. New insights into the regulation of synaptic transmission and plasticity by the endoplasmic reticulum and its membrane contacts. Proc Jpn Acad Ser B Phys Biol Sci. 2021 Dec 10;97(10):559–72.

30. Liu H, Prokosch V. Energy Metabolism in the Inner Retina in Health and Glaucoma. International Journal of Molecular Sciences. 2021 Jan;22(7):3689.

31. Hanna J, David LA, Touahri Y, Fleming T, Screaton RA, Schuurmans C. Beyond Genetics: The Role of Metabolism in Photoreceptor Survival, Development and Repair. Front Cell Dev Biol. 2022 May 18;10:887764.

32. Li S, Sheng ZH. Energy matters: presynaptic metabolism and the maintenance of synaptic transmission. Nat Rev Neurosci. 2022 Jan;23(1):4–22.

33. Perez-Alvarez A, Yin S, Schulze C, Hammer JA, Wagner W, Oertner TG. Endoplasmic reticulum visits highly active spines and prevents runaway potentiation of synapses. Nat Commun. 2020 Oct 8;11(1):5083.

34. Ishikawa M, Iwamoto T, Nakamura T, Doyle A, Fukumoto S, Yamada Y. Pannexin 3 functions as an ER Ca2+ channel, hemichannel, and gap junction to promote osteoblast differentiation. Journal of Cell Biology. 2011 Jun 20;193(7):1257–74.

35. Vanden Abeele F, Bidaux G, Gordienko D, Beck B, Panchin YV, Baranova AV, et al. Functional implications of calcium permeability of the channel formed by pannexin 1. Journal of Cell Biology. 2006 Aug 14;174(4):535–46.

36. Dvoriantchikova G, Ivanov D, Panchin Y, Shestopalov VI. Expression of pannexin family of proteins in the retina. FEBS Letters. 2006;580(9):2178–82.

37. Berry V, Ionides A, Pontikos N, Georgiou M, Yu J, Ocaka LA, et al. The genetic landscape of crystallins in congenital cataract. Orphanet J Rare Dis. 2020 Nov 26;15:333.

38. Song IK, Na S, Paek E, Lee KJ. Cataract-Associated New Mutants S175G/H181Q of βB2-Crystallin and P24S/S31G of γD-Crystallin Are Involved in Protein Aggregation by Structural Changes. Int J Mol Sci. 2020 Sep 5;21(18):6504.

808 39. Cermak T, Doyle EL, Christian M, Wang L, Zhang Y, Schmidt C, et al. Efficient design and
809 assembly of custom TALEN and other TAL effector-based constructs for DNA targeting.
810 Nucleic Acids Res. 2011 Jul;39(12):e82.

811 40. Bedell VM, Wang Y, Campbell JM, Poshusta TL, Starker CG, Krug II RG, et al. In vivo
812 genome editing using a high-efficiency TALEN system. Nature. 2012 Nov;491(7422):114–8.

813 41. Bedell VM, Ekker SC. Using Engineered Endonucleases to Create Knockout and Knockin
814 Zebrafish Models. In: Pruett-Miller SM, editor. Chromosomal Mutagenesis [Internet]. New
815 York, NY: Springer; 2015 [cited 2024 Oct 1]. p. 291–305. Available from:
816 https://doi.org/10.1007/978-1-4939-1862-1_17

817 42. Chen Y, Lun ATL, Smyth GK. From reads to genes to pathways: differential expression
818 analysis of RNA-Seq experiments using Rsubread and the edgeR quasi-likelihood pipeline.
819 F1000Res. 2016;5:1438.

820 43. Chen Y, Chen L, Lun ATL, Baldoni PL, Smyth GK. edgeR 4.0: powerful differential analysis
821 of sequencing data with expanded functionality and improved support for small counts and
822 larger datasets [Internet]. bioRxiv; 2024 [cited 2024 Oct 1]. p. 2024.01.21.576131. Available
823 from: https://www.biorxiv.org/content/10.1101/2024.01.21.576131v1

824 44. Love MI, Huber W, Anders S. Moderated estimation of fold change and dispersion for RNA-
825 seq data with DESeq2 [Internet]. bioRxiv; 2014 [cited 2024 Oct 1]. p. 002832. Available
826 from: https://www.biorxiv.org/content/10.1101/002832v3

827 45. Mudunuri U, Che A, Yi M, Stephens RM. bioDBnet: the biological database network.
828 Bioinformatics. 2009 Feb 15;25(4):555–6.

829 46. Yates B, Gray KA, Jones TEM, Bruford EA. Updates to HCOP: the HGNC comparison of
830 orthology predictions tool. Briefings in Bioinformatics. 2021 Nov 1;22(6):bbab155.

831 47. Szklarczyk D, Kirsch R, Koutrouli M, Nastou K, Mehryary F, Hachilif R, et al. The STRING
832 database in 2023: protein-protein association networks and functional enrichment analyses
833 for any sequenced genome of interest. Nucleic Acids Res. 2023 Jan 6;51(D1):D638–46.

834 48. Wickham H, Averick M, Bryan J, Chang W, McGowan LD, François R, et al. Welcome to the
835 Tidyverse. Journal of Open Source Software. 2019 Nov 21;4(43):1686.

836 49. Choi HMT, Schwarzkopf M, Fornace ME, Acharya A, Artavanis G, Stegmaier J, et al. Third-
837 generation *in situ* hybridization chain reaction: multiplexed, quantitative, sensitive, versatile,
838 robust. Development. 2018 Jun 15;145(12):dev165753.

839 50. Geng Y, Peterson RT. Rapid Mounting of Zebrafish Larvae for Brain Imaging. Zebrafish.
840 2021 Dec;18(6):376–9.

841